

# Scars in the wavefunction: A study of different potential wells using the finite difference method

Ahmed Al-kharusi and Esah Bannister

April 29, 2020

## Abstract

In this report, we study the scars in the wavefunctions of the stadium and Sinai's billiards by using the *finite difference method* (FDM). We compare the scars with the corresponding classical orbitals and estimate the errors in the eigenvalues of the square and circular potential wells as a reference for the error convergence of the eigenvalues. Additionally, we study the level statistics of the half-diamond, rectangle and circle shaped potential wells by comparing their nearest neighbour energy spacing distribution. The energy spacing distribution of the rectangular and circular potential wells, which are integrable systems, were found to follow a Poisson distribution, while the half-diamond shaped potential well followed a *Gaussian orthogonal ensemble* (GOE) distribution. This agrees with the Bohigas-Giannoni-Schmit (BGS) conjecture. Further scars in the wavefunctions of other potential wells are also presented.

## 1 Introduction

For the last 90 years, predictions from quantum mechanics (QM) have been validated in laboratory experiments with incredible accuracy. Where relativistic effects can be ignored QM is the most accurate description of nature today. In the limit of high energies, we expect QM to approach the classical theory formulated by Newton, Lagrange, Hamilton and others. This tendency to classical mechanics at high energies is known as the Bohr's correspondence principle. Quantum systems have wavefunctions with eigenstates which were conjectured to fill the available phase space relatively evenly, with some random fluctuations, particularly at high energies. Counterintuitively, in chaotic quantum systems, unexpected regions with high probability densities emerge within certain wavefunctions. Furthermore, these regions concentrate in the vicinity of unstable periodic orbits of a classical system. These phenomena are known as "scars" and have been observed experimentally in microwave cavities [1], optical cavities [2] [3], and quantum wells [4] [5].

In this report, we use the FDM to solve the two-dimensional time-independent Schrödinger equation (TISE) for arbitrarily shaped potential wells and investigate the properties of scarred wavefunctions which arise from them. We use the numerical results to study the emergent scars in a large energy range and analyse their level statistics.

## 2 Theory

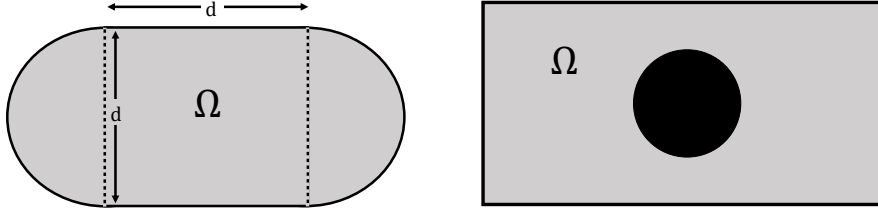


Figure 1: A stadium-shaped potential well (left) consists of a square with semicircles at a pair of opposite sides and a Sinai-shaped potential well (right). The potential is zero inside the shaded region  $\Omega$  and infinite otherwise, including the circle at the centre of the Sinai potential.

If we assume that a frictionless billiard ball is set to bounce around a stadium-shaped table (Figure 1), the motion of the ball will typically follow a non-repeating path, known as ergodic motion since it explores all points on the table. This motion within a stadium billiard can also be described as classically chaotic, i.e. the distance between subsequent trajectories increases exponentially with time. However, for certain initial angles, the ball retraces a similar path over a number of bounces. Such periodic orbits are unstable since a small shift in the motion of the ball will send it onto a non-repeating path once again. Eric Heller considered what would happen if the classical billiard setup were translated into quantum mechanics [6] and he found that certain quantum states have an imprint, or scar, from the periodic orbits within the classical setup. In one of these scarred states, the quantum particle is more likely to be found near an unstable periodic path.

### 2.1 Finite difference method

Quantum scars are only found in non-integrable systems (systems with analytic solution). Therefore, a numerical solution for the TISE is required. The FDM is a method used to solve differential equations numerically. The FDM discretises the independent variable and replaces all partial derivatives in the differential equation with approximations. Using Taylor's theorem,

$$f(x) = \sum_{k=0}^{\infty} f^{(k)}(a) \frac{(x-a)^k}{k!}, \quad (1)$$

if  $f(x)$  has  $m$  continuous derivatives across the interval  $(a, b)$ , then for  $x_0 > a$  and  $x_0 + h < b$ ,

$$f(x_0 + h) = \sum_{k=0}^{m-1} f^{(k)}(x_0) \frac{(h)^k}{k!} + O(h^m). \quad (2)$$

The term  $O(h^m)$  is an error term which is of the order  $h^m$ ,  $x_0$  is the  $x$ -coordinate of a point in the interval  $(a, b)$  and  $h$  represents a small change in the  $x$ -coordinate where  $f$  is evaluated. Truncating equation 2 after the first derivative gives

$$f(x_0 + h) = f(x_0) + hf'(x_0) + O(h^m). \quad (3)$$

Rearranging for  $f'(x_0)$  and neglecting the  $O(h^m)$  term results in

$$f'(x_0) \approx \frac{f(x_0 + h) - f(x_0)}{h}. \quad (4)$$

This is known as the first order forward difference (FD) approximation to  $f'(x_0)$ . In numerical schemes we are restricted to a grid of  $x$  values  $x_1, x_2, x_3, \dots, x_m$ . We will assume a constant grid spacing,  $h$ , in  $x$  so that  $x_{i+1} = x_i + h$ . We will also use the notation,  $f_i = f(x_i)$ , equation 4 therefore becomes

$$f'(x_i) \approx \frac{f_{i+1} - f_i}{h}. \quad (5)$$

The FD approximation for higher order derivatives are derived in a similar manner,

$$\frac{\partial^2 f}{\partial x^2} \approx \frac{f_{i+1} - 2f_i + f_{i-1}}{h^2}. \quad (6)$$

In the FDM, we know the  $f$  values of the TISE at the grid points and want to replace the partial derivatives with differential quotients (6) at these grid points. The TISE is

$$\frac{-\hbar^2}{2m} \left( \frac{\partial^2 \psi}{\partial x^2} + \frac{\partial^2 \psi}{\partial y^2} \right) + V(x, y)\psi = (\hat{\mathcal{H}} + V)\psi = E\psi. \quad (7)$$

where  $\hat{\mathcal{H}}$  is the Hamiltonian operator,  $V(x, y)$  is the potential and  $E$  is the energy eigenvalue for the wavefunction. Consider the points  $x_i$  with  $i = 0, 1, 2, \dots, n$  and  $y_j$  with  $j = 0, 1, 2, \dots, m$  and  $V(x, y) = 0$ . Assuming  $\frac{\hbar^2}{2m} = 1$  and using equation 6, we have

$$\hat{\mathcal{H}}_{i,j} = \frac{\psi_{i+1,j} + \psi_{i-1,j} - 2\psi_{i,j}}{\Delta x^2} + \frac{\psi_{i,j+1} + \psi_{i,j-1} - 2\psi_{i,j}}{\Delta y^2}. \quad (8)$$

This gives us  $n \times m$  finite difference equations with  $n \times m$  unknowns. We can solve this equation using a matrix of the form

$$\begin{pmatrix} \frac{-2}{\Delta x^2} & \frac{1}{\Delta y^2} & 0 & \dots & 0 & \frac{1}{\Delta x^2} & 0 & \dots & \dots & 0 \\ \frac{1}{\Delta y^2} & \frac{-2}{\Delta x^2} & \frac{2}{\Delta y^2} & 0 & \dots & 0 & \frac{1}{\Delta x^2} & 0 & \dots & 0 \\ 0 & \ddots & \ddots & \ddots & 0 & \dots & \dots & \ddots & \dots & 0 \\ \vdots & 0 & \ddots & \ddots & \ddots & 0 & \dots & \dots & \ddots & 0 \\ 0 & \dots & 0 & \ddots & \ddots & \ddots & 0 & \dots & \dots & \ddots \\ \frac{1}{\Delta x^2} & 0 & \dots & 0 & \ddots & \ddots & \ddots & 0 & \dots & 0 \\ 0 & \frac{1}{\Delta x^2} & 0 & \dots & 0 & \ddots & \ddots & \ddots & 0 & \dots \\ \vdots & 0 & \ddots & \dots & \dots & 0 & \ddots & \ddots & \ddots & 0 \\ 0 & \dots & \dots & \ddots & \dots & \dots & 0 & \ddots & \ddots & \ddots \end{pmatrix} \begin{pmatrix} \psi_{0,0} \\ \psi_{0,1} \\ \vdots \\ \psi_{0,n-1} \\ \psi_{1,0} \\ \psi_{1,1} \\ \vdots \\ \psi_{1,n-1} \\ \vdots \\ \psi_{m-1,n-1} \end{pmatrix} = \begin{pmatrix} \hat{\mathcal{H}}_{0,0} \\ \hat{\mathcal{H}}_{0,1} \\ \vdots \\ \hat{\mathcal{H}}_{0,n-1} \\ \hat{\mathcal{H}}_{1,0} \\ \hat{\mathcal{H}}_{1,1} \\ \vdots \\ \hat{\mathcal{H}}_{1,n-1} \\ \vdots \\ \hat{\mathcal{H}}_{m-1,n-1} \end{pmatrix} \quad (9)$$

## 2.2 Chaotic systems and the BGS conjecture

Scars were originally discovered through the study of quantum chaos, which studies how classically chaotic dynamical systems can be described in terms of quantum theory [6]. The concept of chaos is associated with the notion of sensitivity to initial conditions and the exponential divergence of subsequent trajectories.

The BGS conjecture reveals that a strong link exists between chaos, which is a concept of classical mechanics, and random matrix theory-where a random matrix is a matrix in which some or all elements are random variables. More specifically that the spectral fluctuation properties of chaotic systems with unknown Hamiltonians can be predicted using ensembles of random matrices [7] [8].

The systems which the BGS conjecture can describe are simple quantum mechanical systems for which one can define a classical limit, such as the two-dimensional quantum billiard mentioned

previously. For instance, the spectral statistics of Sinai's billiard could be described by random matrix ensembles [9]. Depending on the symmetry with respect to time-reversal, one can completely specify the random matrix ensemble to construct. In the case of the two-dimensional billiard, subject to the fact that the system is invariant under time-reversal symmetry with integer spin, this corresponds to the GOE distribution [10].

The main difference between the integrable systems and non-integrable systems is the distribution of their energy spacing. The BGS conjecture predicts that the nearest neighbour *energy spacing distribution* (ESD) of integrable systems follows a Poisson distribution, while ESD for non-integrable systems follow a GOE distribution [11]. The mathematical expression of the GOE distribution,  $P(s)$ , is given by

$$P(s) = \frac{\partial^2}{\partial s^2} \left[ \operatorname{erfc} \left( \frac{\sqrt{\pi}s}{2N} \right) \right]^N, \quad (9)$$

where  $s$  is the energy spacing and  $\operatorname{erfc}$  is the complementary error function [12]. We will refer to this equation by GOE for  $N = 1$  and by GOE2 for  $N = 2$ . The expression of the GOE distribution can be compared with the analytic energy spacing distribution of the system. The energy eigenvalues for the rectangular and circular potentials are

$$E_{n_x, n_y} = \frac{\hbar^2 \pi^2}{2\mu} \left( \frac{n_x^2}{L_x^2} + \frac{n_y^2}{L_y^2} \right) \quad (10)$$

$$E_{m, n_r} = \frac{\hbar^2}{2\mu R^2} [z_{m, n_r}]^2, \quad (11)$$

respectively, where  $\mu$  is the mass of the particle in the potential and the subscripts represent the quantum numbers. In equation 10,  $L_x$  and  $L_y$  represent the length of sides of the rectangle. In equation 11,  $R$  is the radius of the circle and  $z_{m, n_r}$  is the  $n_r^{th}$  zero of the regular Bessel function,  $J_{m(z)}$  [13].

## 3 Method implementation

### 3.1 Solving the TISE in Python

The method used in this report to construct the Hamiltonian matrix can be readily applied to any arbitrarily shaped potential. First, the potential well was plotted as shown in Figure 2 (a). Using the FDM, the coordinate system was divided into small squares each of area  $h^2$ . We refer to these squares as *pixels*. This was then used to construct a matrix which is referred to as the *coordinate matrix*. Each pixel in the coordinate system corresponds to an element in the coordinate matrix. Furthermore, if a pixel lies in an area where the potential is zero it is recorded as 0 in the coordinate matrix; otherwise, it is recorded as 1. This is illustrated in Figure 2. For a general potential well, the coordinate matrix can be constructed by transforming an image (in black and white) of the potential well (e.g. Figure 2 (a)) into a binary matrix (i.e. each element = 0 or 1) using the Python language [14] [15].

Then the Hamiltonian matrix, which is a square matrix of rows = columns =  $M \times N$ , was constructed. Each pixel in the coordinate matrix has a corresponding row in the Hamiltonian matrix. Let the first row in the Hamiltonian matrix correspond to the pixel with coordinates (row, column) =  $(N, 1)$  in the coordinate matrix, the  $N^{th}$  pixel to  $(1, 1)$ , the  $(N + 1)^{th}$  pixel to  $(N, 2)$  and so on. The pixels were labeled from bottom to top and from left to right in Figure 2 (b). Likewise, the wavefunctions corresponding to each pixel were labeled in the coordinate matrix with the pixel's coordinate (e.g.  $\psi_{M,N}$ ).

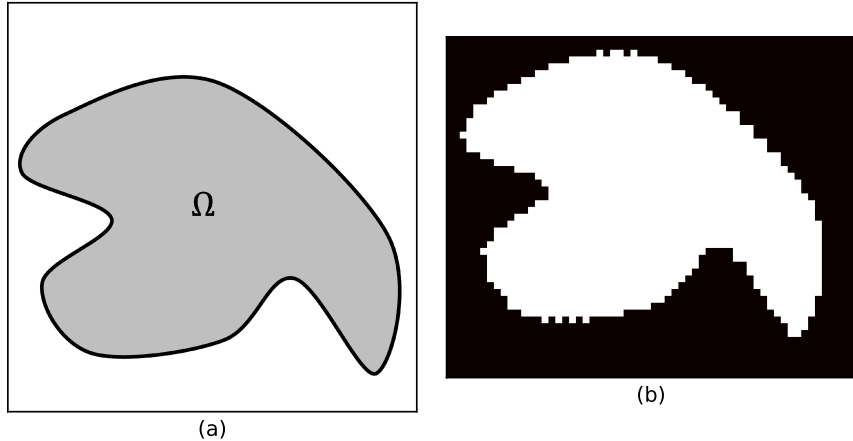


Figure 2: The sketch of the potential well (a) and the corresponding coordinate matrix (b). The potential is zero inside the region  $\Omega$ . In (b), the black region represents pixels = 0, while the white region represents pixels = 1.

For a given row, the maximum value of a non-zero element in the Hamiltonian matrix is five. This corresponds to a pixel inside the region  $\Omega$  (see Figure 2 (a)) where there are contributions from the neighbouring pixels (above, below, left and right) in the coordinate matrix. This does not hold for a boundary point. To find the elements of a general row, a 1D array is constructed from the coordinate matrix. This is constructed such that the  $N^{th}$  pixel corresponds to the  $N^{th}$  row in the Hamiltonian matrix. For a general row, if the corresponding pixel is 0 (i.e. outside  $\Omega$ ), then the row will have no contributions. If the  $i^{th}$  pixel is 1, we check  $(i - 1)^{th}$  and  $(i + 1)^{th}$  elements in the 1D array for the contributions from the pixels above and below and similarly we check  $(i - N)^{th}$  and  $(i + N)^{th}$  elements in the 1D array for the contributions from the left and right. This is illustrated in Figure 3. Finally, the Python language was used to find the eigenvalues (the energies) and the eigenvectors (the wavefunctions). This Python file was then compiled to an executable file which can be used to find the scars in an arbitrary shaped infinite potential well [16].

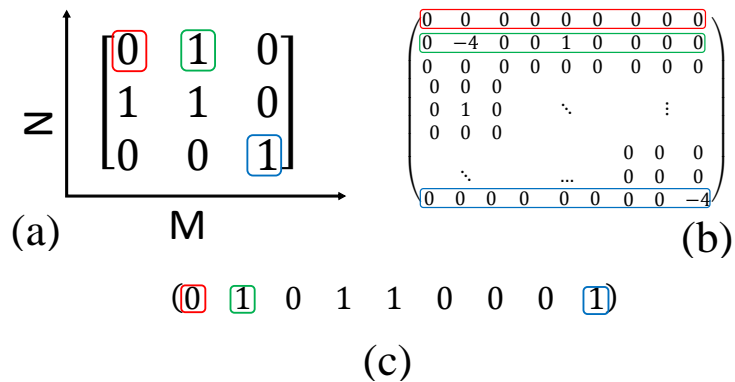


Figure 3: An example of a coordinate matrix (a), the corresponding Hamiltonian matrix (b) and the 1D array (c) constructed using (a). For illustration, some pixels in (a) and their corresponding rows/elements in (b) and (c) are marked with the same colour.

### 3.2 Creating a classical simulation

To confirm the classical attributes of the scars a simulation [17] of a light ray was used within a series of mirrors shaped with the same dimensions as the billiard as shown in Figure 1. The path of the light ray within a stadium shaped mirror was used to model the classical path of a particle. The optical set-up was also used to predict the nature of scars which were yet to be identified. Due to the instability of the periodic orbits corresponding to the scars, the mirrors could not completely enclose the stadium shape as the light ray would escape the orbit and form a different pattern.

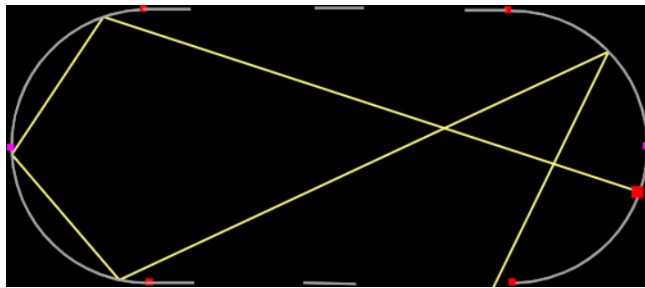


Figure 4: An example of a classical simulation in a stadium-shaped billiard. The larger red box marks the beginning of the light ray, which is to be reflected within a series of shaped mirrors which model a stadium billiard. The smaller coloured boxes are used to adjust the shape of the billiard to simulate different potential wells.

## 4 Results

### 4.1 Stadium billiard

The plots in Figure 5 depict the probability density for a free quantum particle in the stadium in different energy states. A number of scars were identified within the stadium billiard, corresponding to a wide range of unstable classical orbits. The results are therefore in agreement with the correspondence principle. One of the most frequent scars was that of a particle tracing the shape of a rectangle in its classical periodic orbit (Figure 5, right, iii). With closer inspection, other clear scars such as a bow-tie (Figure 5, right, iv) and similar variants (Figure 5, right, i/ii) were also noted. At low energy levels, it was difficult to distinguish between different types of scars, particularly the scars corresponding to Figure 5 ii/iv as well as Figure 5 i/v. It was, therefore, necessary to identify specific types of scars present at relatively high energy states and then search at lower energy states for any reoccurrences of such scars. An interesting feature to note is the multiple independent orbits displayed in (Figure 5, right v) which are classically impossible. The resolution used in this numerical experiment is  $262 \times 131$  pixels and the total number of eigenstates found were 34322.

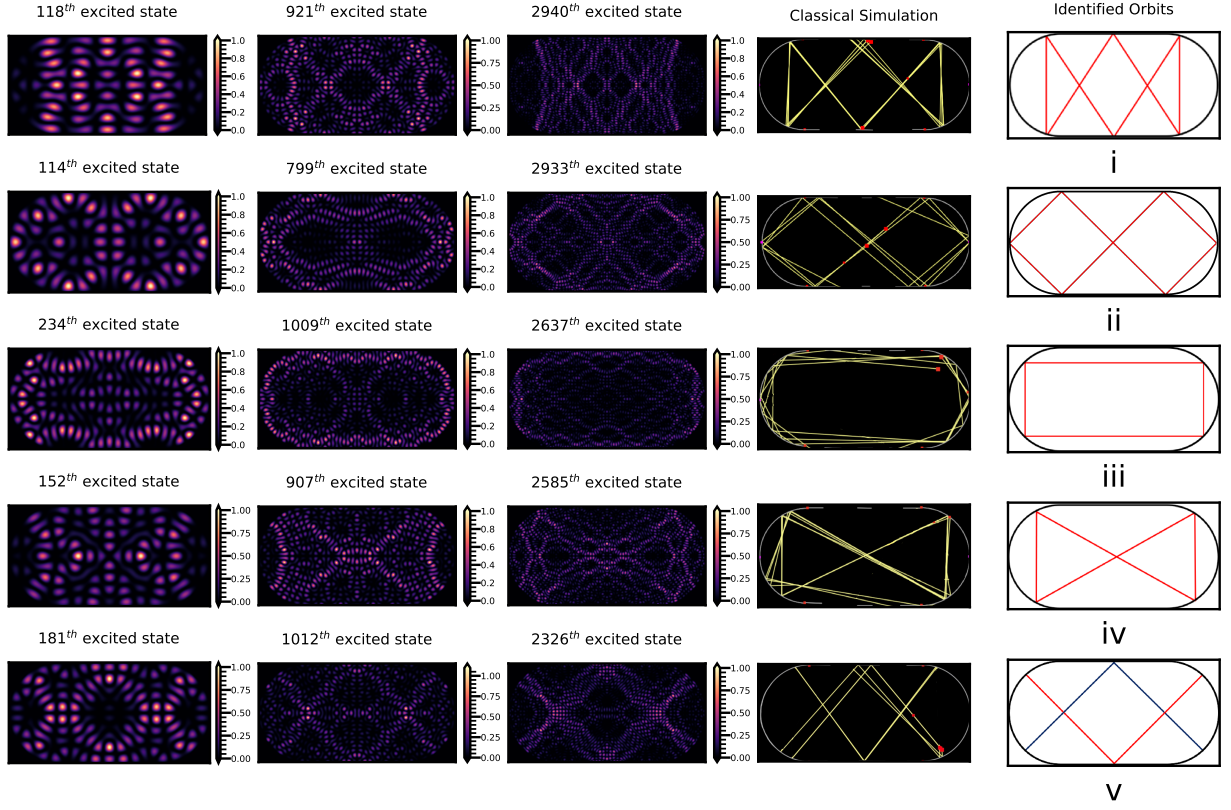


Figure 5: Scars in the wavefunction of the stadium billiard. On the left are the probability density plots for a number of scarred states in the stadium billiard. To the right, the classical simulations of the scars using a light ray within a series of mirrors in the shape of a stadium billiard. The plots to the far right are the corresponding classical orbit identified from the simulation. The values in the colour bar indicate the unnormalized probabilities.

## 4.2 Sinai's billiard

Figure 6 shows the scars of the wavefunction in Sinai's billiard with the corresponding classical orbitals. As hypothesized, the scars are clearer in the limit of high energies (the classical limit). As in the stadium, in some eigenstates, the scars correspond to a superposition of classical orbitals, while in others they correspond to a single classical orbital as depicted in Figure 6. The results generally agree with the findings of Sridhar and Lu [18]. The resolution used in this numerical experiment is  $262 \times 131$  pixels and the total number of eigenstates found were 34322.

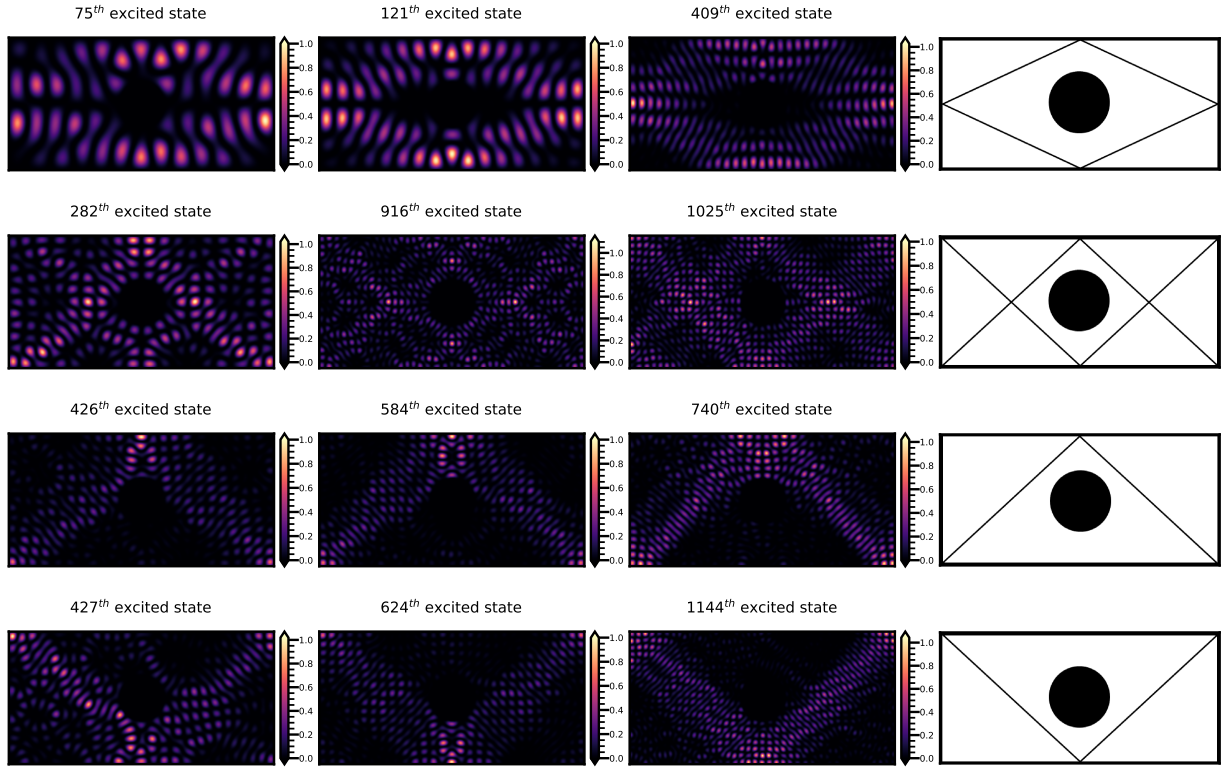


Figure 6: Scars in the wavefunction of the Sinai's billiard. The probability densities are on the left and the corresponding classical orbitals are on the right. The values in the colour bar indicate the unnormalized probabilities.

### 4.3 Level statistics and error convergence

Since there is no analytic solution for this system, the uncertainties of the eigenvalues cannot be found directly by comparing the results with the analytic solution. Therefore, to see how the results of FDM converges with the resolution, the errors of the eigenvalues for the square and circular potential wells are plotted in Figure 7. This figure shows that higher resolutions are closer to the analytic solution as expected for the FDM. The figure also indicates that the convergence of the results for the square potential is much faster than that for the circular potential. This is mainly because of the boundary points which are more complicated for the circular potential, in particular it is easier to represent a shape of a square with fewer pixels. Furthermore, Figure 7 shows that using  $100^2$  pixels, the error at the  $1400^{th}$  energy state is approximately 10%, while for the circular potential with the same resolution the error in the  $1400^{th}$  energy state is approximately 90%.

The errors in Figure 7 were found by constructing a 1D array of the sorted eigenvalues and another 1D array of the analytic energies. Thus, by comparing these arrays, the relative error can be deduced. The error of the circular potential well shows a sharp increase (see Figure 7) after the ground state. This might be because for some of the eigenstates, more than one numerical eigenvalue were found to correspond to that state. These were not degenerate but are the same to approximately 8 significant figures. Since the errors were deduced by subtracting successive elements of the 1D arrays, this did not result in the correct error. To reduce the effect of this, the 1D arrays were rounded to 6 significant figures. Following this, the elements with the same energies were removed from the arrays. The errors for the circular potential in

Figure 7 correspond to the results after the approximation and yet the issue is not fully resolved. A further approximation will result in a lower precision. It is therefore concluded that the error estimation for the circular potential presented in Figure 7 is not accurate.

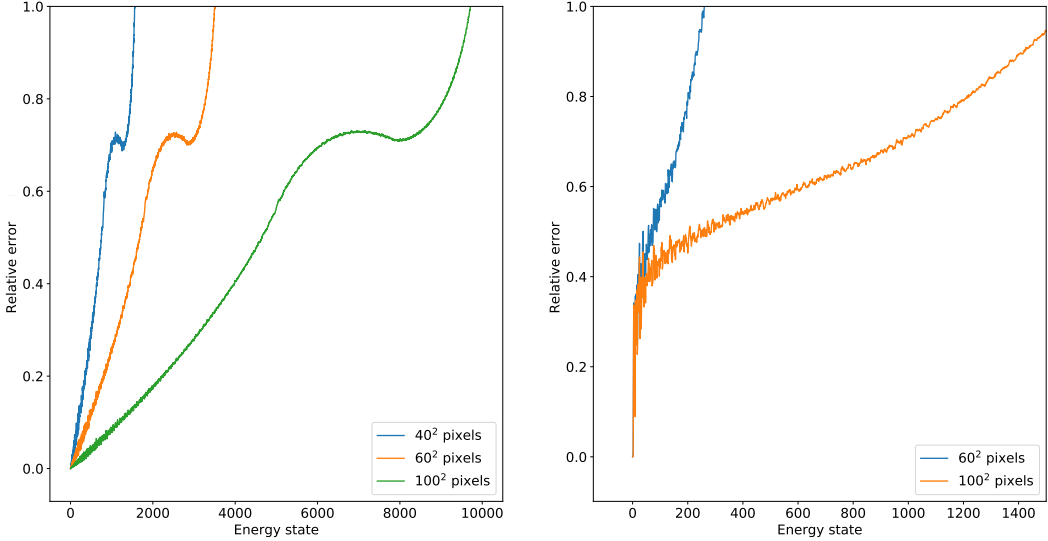


Figure 7: The relative errors for the square (left) and circular (right) potential wells at different resolutions. The relative error is the ratio of the difference between the numerical and analytic eigenvalues to the numerical eigenvalues.

The ESD of the rectangle, half-diamond and circle shaped potential wells are shown in Figure 8. These were found by sorting the eigenvalues of each potential and calculating the difference between the successive eigenvalues. In agreement with the BGS conjecture, the ESD of the rectangular and circular potential wells followed a Poisson distribution, whereas the ESD of the half-diamond shaped potential followed a GOE distribution [19] [20]. The ESD for non-integrable systems follows different types of GOE distributions according to the symmetry of the system, in particular odd wavefunctions follow GOE [12]. Therefore, the half-diamond shaped potential was used. In contrast, the diamond potential follows GOE2 distribution [12]. All the eigenvalues were used to plot the distributions in Figure 8. Although the eigenvalues corresponding to high energy values are not accurate, the purpose was to show the general ESD.

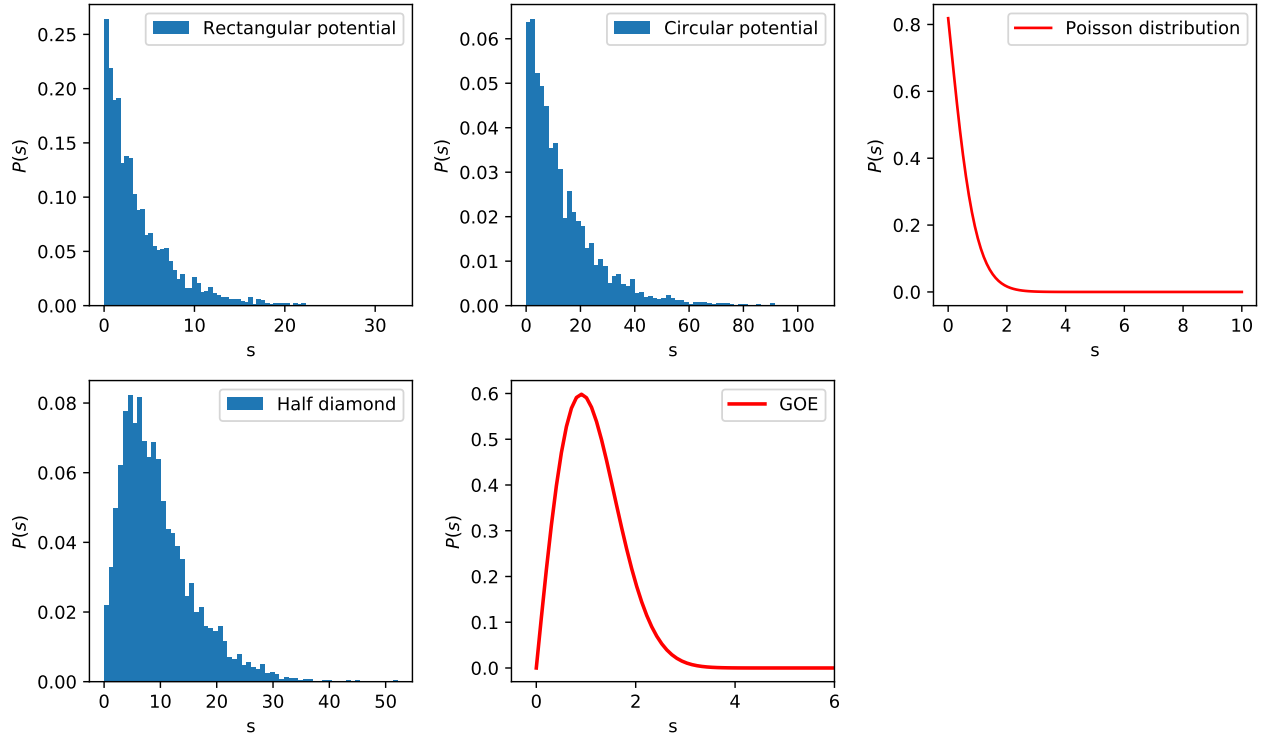


Figure 8: The ESD of the rectangle and half diamond potential wells (blue) and the corresponding distribution according to the BGS conjecture (red). The area under the histograms are normalized to unity and the units for the energy spacing,  $s$ , is arbitrary.

The scars in the wavefunction of an arbitrarily shaped potential might be harder to identify. An example of this is shown in Figure 9, further scars for this and other shaped potentials are included in appendix A. This also illustrates the generality of the method used in this report.

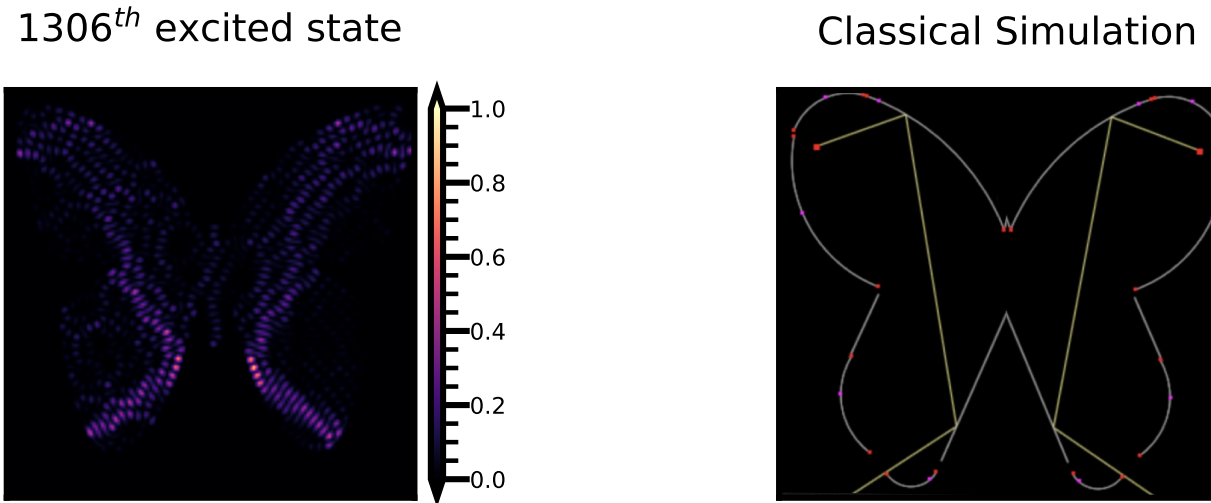


Figure 9: A scar in the wavefunction of the butterfly-shaped potential well. The values in the colour bar indicate the unnormalized probabilities.

## 5 Conclusion

In conclusion, we have shown the scars in the wavefunctions of the stadium and Sinai's billiards using the FDM. Each scar was compared with a corresponding unstable classical periodic orbital using a classical simulation. The errors in the eigenvalues of the square and circular potential wells, when estimated, showed that the results of FDM converged with increasing resolution. The level statistics of the half-diamond, rectangle and circular shaped potential wells were studied by comparing their nearest neighbour energy spacing distribution. These were in agreement with the BGS conjecture. Furthermore, the generality of the method used in this report enabled us to study the scarring of arbitrarily shaped potential wells and we presented, for illustration, the scars in the butterfly, annulus and diamond shaped potentials. This work can be extended by considering the time evolution of a superposition of the eigenstates. Additionally, the method used in this report to construct the Hamiltonian matrix can be extended to 3D. In this case, the shape of the potential in 3D can be constructed by taking the volume of revolution of the 2D potential.

## References

- [1] S. Sridhar, "Experimental observation of scarred eigenfunctions of chaotic microwave cavities," *Physical review letters*, vol. 67, no. 1, p. 785, 1991.
- [2] S.-B. Lee, J.-H. Lee, J.-S. Chang, H.-J. Moon, S. W. Kim, and K. An, "Observation of scarred modes in asymmetrically deformed microcylinder lasers," *Physical review letters*, vol. 88, no. 3, p. 033903, 2002.
- [3] T. Harayama, T. Fukushima, P. Davis, P. O. Vaccaro, T. Miyasaka, T. Nishimura, and T. Aida, "Lasing on scar modes in fully chaotic microcavities," *Physical Review E*, vol. 67, no. 1, p. 015207, 2003.
- [4] T. Fromhold, P. Wilkinson, F. Sheard, L. Eaves, J. Miao, and G. Edwards, "Manifestations of classical chaos in the energy level spectrum of a quantum well," *Physical review letters*, vol. 75, no. 6, p. 1142, 1995.
- [5] P. Wilkinson, T. Fromhold, L. Eaves, F. Sheard, N. Miura, and T. Takamasu, "Observation of 'scarred' wavefunctions in a quantum well with chaotic electron dynamics," *Nature*, vol. 380, no. 6575, pp. 608–610, 1996.
- [6] E. J. Heller, "Bound-state eigenfunctions of classically chaotic hamiltonian systems: Scars of periodic orbits," *Physical Review Letters*, vol. 53, no. 16, p. 1515, 1984.
- [7] G. Casati, F. Valz-Gris, and I. Guarnieri, "On the connection between quantization of nonintegrable systems and statistical theory of spectra," *Lettore al Nuovo Cimento*, vol. 28, no. 8, pp. 279–282, 1980.
- [8] J.-C. Gay, *Irregular atomic systems and quantum chaos*. CRC Press, 1992.
- [9] J.-F. Laprise, A. Hosseini-zadeh, H. Kröger, *et al.*, "Universality in statistical measures of trajectories in classical billiard systems," *Applied Mathematics*, vol. 6, no. 08, p. 1407, 2015.
- [10] S. W. McDonald and A. N. Kaufman, "Spectrum and eigenfunctions for a hamiltonian with stochastic trajectories," *Physical Review Letters*, vol. 42, no. 18, p. 1189, 1979.
- [11] T. Kriecherbauer, J. Marklof, and A. Soshnikov, "Random matrices and quantum chaos," *Proceedings of the National Academy of Sciences*, vol. 98, no. 19, pp. 10531–10532, 2001.

- [12] R. P. Salazar, G. Tellez, D. F. Jaramillo, and D. L. Gonzalez, “Chaos in the diamond-shaped billiard with rounded crown,” *Revista de la Academia Colombiana de Ciencias Exactas, Fisicas y Naturales*, vol. 39, no. 151, pp. 152–170, 2015.
- [13] C. W. David, “The particle in a box (and in a circular box),” 2006.
- [14] I. W. Sudiarta and D. W. Geldart, “Solving the schrödinger equation using the finite difference time domain method,” *Journal of Physics A: Mathematical and Theoretical*, vol. 40, no. 8, p. 1885, 2007.
- [15] R. Becerril, F. Guzmán, A. Rendón-Romero, and S. Valdez-Alvarado, “Solving the time-dependent schrödinger equation using finite difference methods,” *Revista mexicana de fisica E*, vol. 54, no. 2, pp. 120–132, 2008.
- [16] A. Al-kharusi and E. Bannister, *Schrodinger eq solver 1.0. accessed on: Apr. 25, 2020. [online]. available:<https://github.com/ahmed-alkharusi/schrodinger-eq-solver-1.0>*, 2020.
- [17] R. Tu, “Ray optics simulation. accessed on: Apr. 18, 2020. [online]. available: [Https://github.com/ricktu288/ray-optics](https://github.com/ricktu288/ray-optics),” 2018.
- [18] S. Sridhar and W. Lu, “Sinai billiards, ruelle zeta-functions and ruelle resonances: Microwave experiments,” *Journal of statistical physics*, vol. 108, no. 5-6, pp. 755–765, 2002.
- [19] D. Kauffman, I. Kosztin, and K. Schulten, “Expansion method for stationary states of quantum billiards,” *Am. J. Phys*, vol. 67, pp. 133–141, 1999.
- [20] Z. Rudnick, “Quantum chaos?” *Notices of the AMS*, vol. 55, no. 1, pp. 32–34, 2008.

# Appendix A

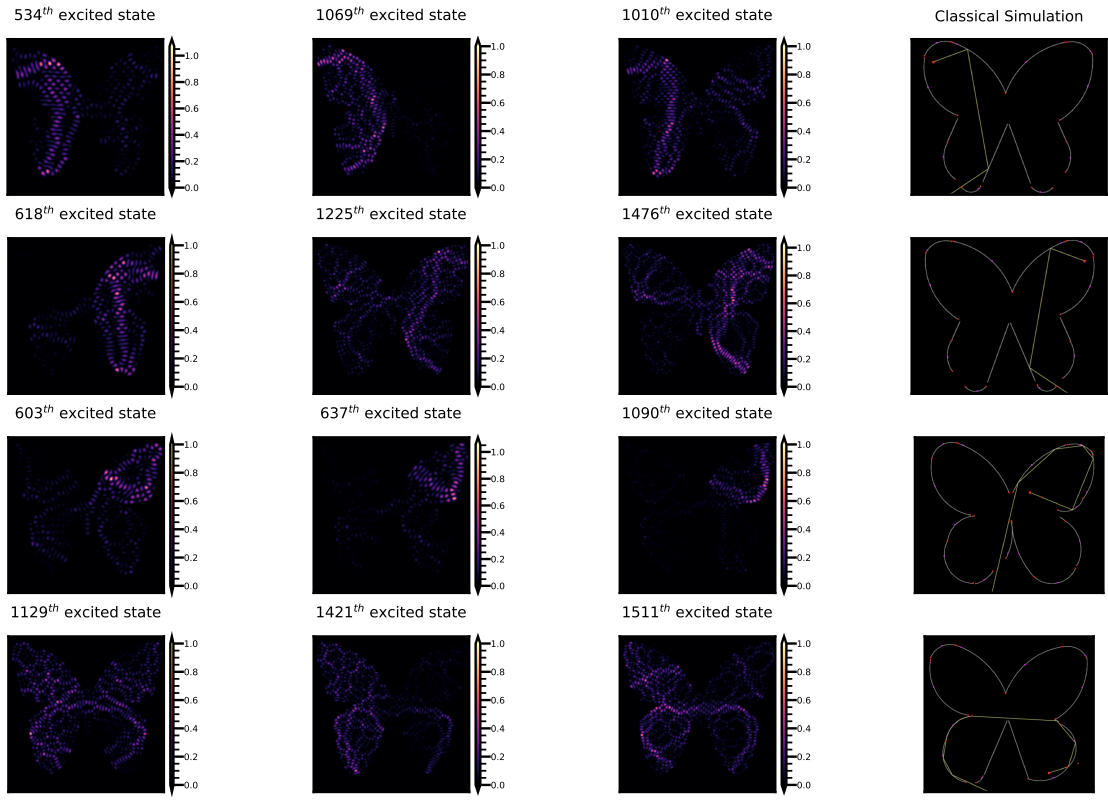


Figure 10: Scars in the wavefunction of the butterfly shaped potential well, the resolution is  $151 \times 151$  pixels. The values in the colour bar indicate the unnormalized probabilities.

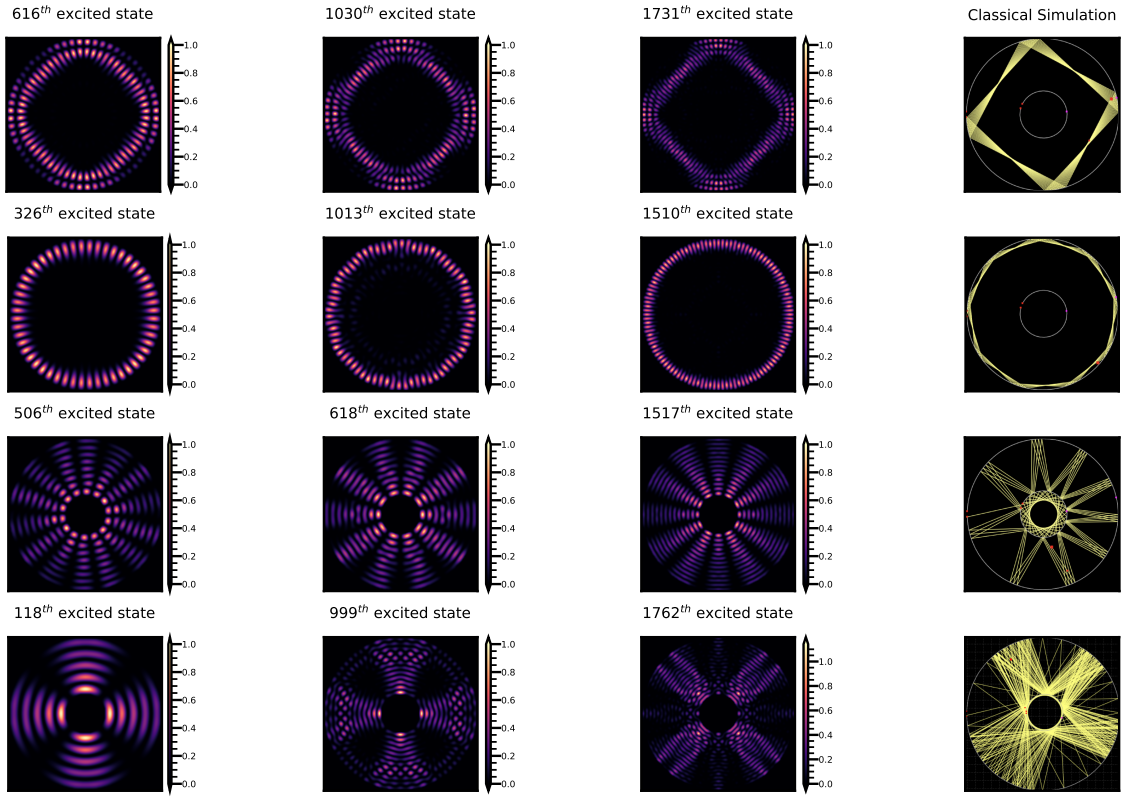


Figure 11: Scars in the wavefunction of the annulus-shaped potential well, the resolution is  $151 \times 151$  pixels. The values in the colour bar indicate the unnormalized probabilities.

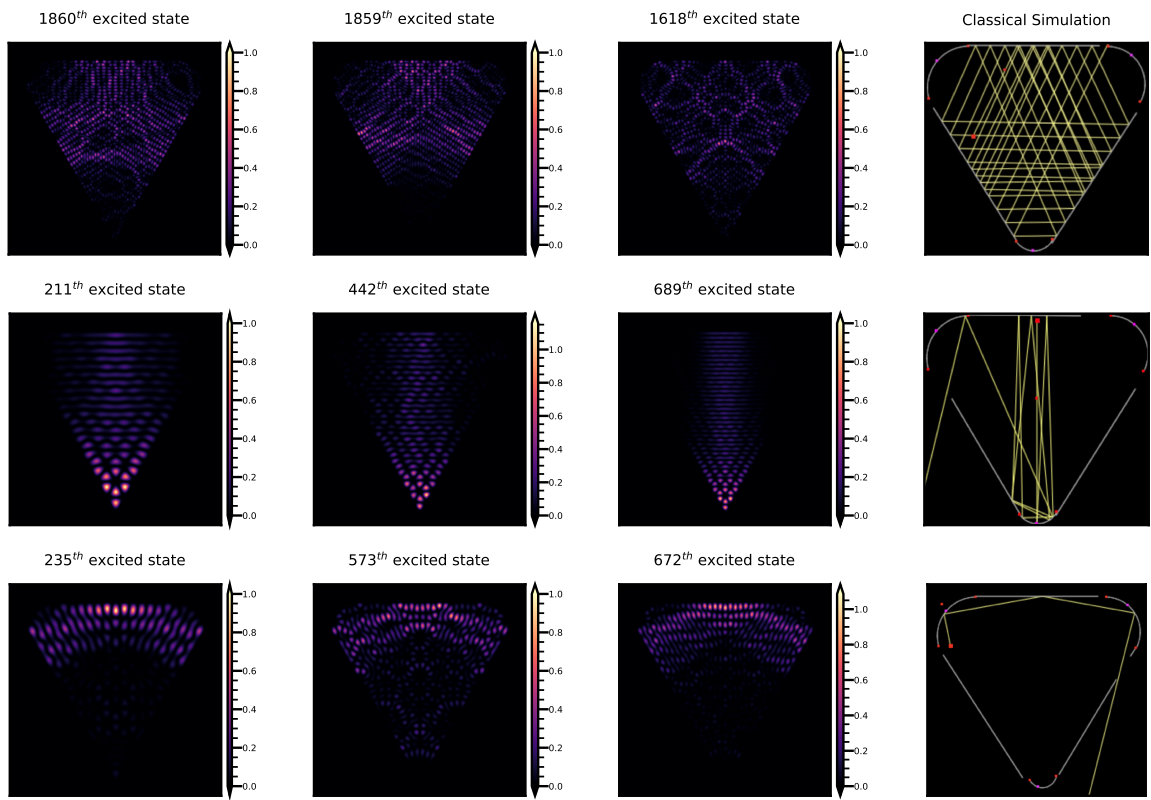


Figure 12: Scars in the wavefunction of the diamond-shaped potential well, the resolution is  $181 \times 181$  pixels. The values in the colour bar indicate the unnormalized probabilities.